ELSEVIER

Contents lists available at ScienceDirect

# Journal of Power Sources

journal homepage: www.elsevier.com/locate/jpowsour





# Perovskite films passivated by a dendrimer toward high efficiency and high stability devices

Yifang Qi<sup>a</sup>, Mahesh Loku Yaddehige<sup>b</sup>, Kevin A. Green<sup>c</sup>, Jaiden Moore<sup>a</sup>, Surabhi Jha<sup>c</sup>, Guorong Ma<sup>c</sup>, Chen Wang<sup>d</sup>, Davita L. Watkins<sup>b</sup>, Xiaodan Gu<sup>c</sup>, Derek Patton<sup>c</sup>, Sarah E. Morgan<sup>c</sup>, Qilin Dai<sup>a,\*</sup>

- <sup>a</sup> Department of Chemistry, Physics, and Atmospheric Sciences, Jackson State University, Jackson, MS, 39217, United States
- <sup>b</sup> Department of Chemistry and Biochemistry, The University of Mississippi, University, MS, 38677, United States
- <sup>c</sup> School of Polymer Science and Engineering, Center for Optoelectronic Materials and Devices, The University of Southern Mississippi, Hattiesburg, MS, 39406, United States
- d Department of Chemistry and Biochemistry, Queens College, City University of New York, Flushing, NY, 11367, United States

#### HIGHLIGHTS

- We design a dendrimer, fatty acid-polyamidoamine -COOH (FPC).
- FPC has sixteen long alkyl chains and eight carboxylic acid functional groups.
- FPC is a hyperbranched polymer capable of self-assembling in water.
- The functional groups of FPC increase the performance of perovskite solar cells.

# ARTICLE INFO

Keywords: Perovskite solar cells Passivation Polymer Alkyl chains Stability

#### ABSTRACT

Passivation engineering has become one of the most effective and convenient strategies to enhance the performance and the stability of perovskite solar cells (PSCs). We design a new material, fatty acid-polyamidoamine-COOH (FPC), with sixteen long alkyl chains and eight carboxylic acid functional groups. The carboxylic acid can passivate the Pb defects at the surface and grain boundaries (GBs). Self-arrangement of the FPC molecules on the surface results in improved surface potential. FPC passivation leads to suppressed charge recombination, enhanced charge carrier transport, and increased light-harvesting. The transient absorption measurements confirm the key role of FPC passivation on the recombination at the interface between perovskite and PC<sub>61</sub>BM layer in PSCs. The power conversion efficiency (PCE) of PSCs modified by FPC increases to 21.01% with Jsc 23.74 mA/cm², Voc 1.09 V, and FF 81.16%. Furthermore, the hydrophobic long alkyl chains improve the device stability. Under 60  $\pm$  5% relative humidity (RH), the PSCs with FPC passivation maintain  $\sim$ 90% of the initial PCE for 3500 min, but the control PSCs only keep  $\sim$ 50% of the origin PCE. In addition, the devices modified by FPC could maintain  $\sim$ 82% of the initial PCE value under 25  $\pm$ 5% (RH) and 30  $\pm$ 5 °C ambient environment for 30 days. This work provides a guideline for designing passivants to improve the efficiency and stability of devices.

#### 1. Introduction

Perovskite solar cell devices (PSCs) are considered to be the next-generation solar cells owing to their excellent optoelectronic properties, such as the strong light-harvesting, tunable bandgaps, low cost, and solution processability [1–3]. In the past decade, PSCs have shown

remarkable progress in the solar cell field, and the power conversion efficiency (PCE) of regular structure PSCs has already reached 25.7% [4]. The inverted structure PSCs exhibit advantages over the regular structure PSCs such as low-cost, non-hysteresis, low-temperature fabrication [5], roll-to-roll manufacture, and flexible device production [6–9]. However, the highest PCE of the inverted structure PSCs is still

E-mail address: qilin.dai@jsums.edu (Q. Dai).

<sup>\*</sup> Corresponding author.

lower than the regular structure [10]. The high-density defect states caused by the solution process to fabricate perovskite films significantly influence the performance and stability of the devices [11–14]. Theoretical and experimental results have shown that surface trap states are extremely detrimental to the performance of PSCs [15–17]. Besides, PSC device stability, which is also related to the defects, is another issue for practical applications due to the properties of perovskite films. Therefore, defect passivation is considered to be a very promising way to improve the device performance of inverted PSCs.

Many effective strategies have been developed to passivate the defects and enhance the PSC performance, including device interface passivation and perovskite precursor engineering [18–21]. Limited progress has been made by perovskite precursor engineering since the original perovskite film growth process cannot be disturbed. Therefore, only several solvents and solutes are available for perovskite film growth. Defect passivation has been proven to be an effective way to improve the PSC performance due to the interaction between the perovskite films and passivation additives [22]. Many kinds of passivation additives in perovskite film have been studied, such as ionic liquids, small organic molecules, ammonium salts, Lewis acid, Lewis base, and polymers [11,15,23–28].

Recently, small organic molecules with numerous functional groups to suppress carrier recombination and decrease the trap density of perovskite films have attracted much attention [29]. Wei Chen et al. reported conjugated small molecules (bithiophene imide) to enhance the device PCE from 18.89% to 20.67%, due to the defect passivation by -SH functional groups [30]. Chih-Yu Chang et al. improved the PCE from 19.19% to 20.30% by thiazole-bridged diketopyrrolopyrrole -based semiconducting molecules [31]. However, small organic molecules may introduce traps in the interconnection, which would limit the passivation effect in perovskite films [32]. Compared to small organic molecules, large molecule polymers have a preferential orientation along grain boundary for perovskite film passivation, which can mitigate the introduction of the traps [33]. Furthermore, the moisture invasion can induce a fast degradation in the grain boundaries of the perovskite films [34,35]. Thus, the PSCs with hydrophobic polymer passivation show enhanced moisture stability. Although PSCs with polymer passivation exhibit a large number of advantages, few studies are related to the multifunctional passivation of polymers including defect passivation, enhanced charge extraction and transport, reduced charge recombination, and enhanced stability under moisture environment.

Han et al. applied an organic dye to improve the performance of PSCs via the interaction between the under-coordinated Pb2+ ions and the -COOH functional groups of the organic dye [36]. Xiong et al. introduced 3-(2-benzimidazolyl)-7-(diethylamino)-coumarin into perovskite films to improve the stability of the devices via the interaction of the functional groups of -COO and Pb<sup>2+</sup> ions in perovskite films [37]. Islam et al. employed 5-ammonium valeric acid iodide as a passivation additive to enhance the stability of PSCs due to the -COOH and NH<sub>3</sub><sup>+</sup> function group of 5-AVAI [38]. Li et al. utilized sodium dodecylbenzene sulfonate with the hydrophobic long alkyl chain to enhance the stability of PSCs, which could keep over 90% of its initial PCE values after 90 days [39]. Dong et al. passivated perovskite films by cetyltrimethylammonium bromide to improve the stability of the devices due to the hydrophobic long alkyl chains [40]. Therefore, -COOH can passivate the defects of the perovskite films to improve the corresponding device efficiency, and long alkyl chains can improve the stability of PSCs due to their hydrophobic properties. Thus, it is a promising strategy to boost both the efficiency and the stability of the devices via one passivation additive with both -COOH and long alkyl chains. The number of -COOH groups and long alkyl chains in one molecule are critical to the passivation effect. The more functional groups, the better passivation effect. However, it is challenging to commercially obtain a material with large numbers of -COOH groups and long alkyl chains.

Herein, we design a dendrimer, fatty acid-polyamidoamine -COOH

(FPC) with sixteen long alkyl chains and eight carboxylic acid functional groups to improve the performance of the inverted PSCs. It is a hyperbranched polymer capable of self-assembling in the presence of water due to the functional groups [41]. We study the multifunctional passivation of FPC in PSCs. The FPC passivation not only enhances the PCE of PSCs from 18.71% to 21.01% but also protects devices from moisture erosion and suppresses the ion migration at the interface between perovskite and electron transport layer, thus further improving the stability in the high moisture environment. The Voc improvement of PSCs is related to the reduced nonradiative recombination due to the decreased traps at the surface and GBs of the perovskite layer after FPC modification. The PSCs with FPC maintain  $\sim 90\%$  of the initial PCE under 60  $\pm$  5% relative humidity (RH) for 3500 min, and the control devices only keep ~50% of the original values. The mechanism of the improved device performance by FPC passivation is studied. FPC passivation effectively reduces the surface defects and GB defects in PSCs due to the eight carboxylic acid functional groups, and FPC improves the device stability via sixteen long alkyl chains.

#### 2. Materials and methods

#### 2.1. Materials

The details about the dendrimer fatty acid (FA)-polyamidoamine (PAMAM)-COOH (FPC) were reported in our previous work [41]. Poly [bis(4-phenyl) (2,4,6-trimethylphenyl) amine] (PTAA, >99%) was received from Solaris Chem (Canada) [6,6].-phenyl C61-butyric acid methyl ester (PC $_{61}$ BM, 99.5%) was purchased from Nano C Crop (USA). Methylammonium iodide (MAI, 99.5%), N, N-Dimethylformamide (DMF, Anhydrous 99.8%), isopropanol (IPA, Anhydrous 99.5%) and chlorobenzene (CB, Anhydrous 99.8%) were obtained from Sigma-Aldrich (USA). Dimethyl sulfoxide (DMSO, Anhydrous 99.8%), bathocuproine (BCP) and lead iodide (PbI $_{2}$ , 99%) were purchased from Alfa Aesar (USA). Patterned ITO glass substrates (7–9  $\Omega$ /sq) were received from Advanced Election Technology Co., Ltd (China).

#### 2.2. Device fabrication

Firstly, ITO glass substrates were cleaned by soap, deionized water, acetone, and IPA, sequentially. PTAA as hole transport layer with the concentration of 3 mg/mL in CB was spin-coated on substrates at 4000 rpm for 30 s, then the substrates were annealed at 100  $^{\circ}$ C for 10 min. The perovskite precursor solution was prepared by 1.2 M PbI<sub>2</sub> and 0.3 M MAI in mixed solvents (DMF: DMSO = 1:10). The wet perovskite films were prepared by a two-step method. First, the perovskite precursor solution was spin-coated with 6000 rpm for 20 s, then MAI solution (30 mg/mL in IPA) was spin-coated with 4000 rpm for 40 s. The wet films were annealed at 100 °C for 30 min to form the ITO/PTAA/MAPbI<sub>3</sub> films. FPC in IPA was spin-coated on the top of ITO/PTAA/MAPbI3 films at 4000 rpm for 30 s, and the ITO/PTAA/MAPbI<sub>3</sub>/FPC films were annealed for 70 °C for 10 min. For the electron transport layer, PC<sub>61</sub>BM (20 mg/mL in CB) was spin-coated on the ITO/PTAA/MAPbI<sub>3</sub>/FPC films with 3000 rpm for 30 s. Then the  $ITO/PTAA/MAPbI_3/FPC/PC_{61}BM$  films were annealed at 90  $^{\circ}\text{C}$  for 30 min. Afterwards, BCP (0.5 mg/mL in IPA) was spin-coated onto  $PC_{61}BM$  with 4000 rpm for 30 s. Finally, Ag electrode was evaporated under a vacuum of  $6 \times 10^{-4}$  Pa to finish device fabrication. Thus, the structure of the PSCs is ITO/PTAA/MAPbI<sub>3</sub>/FPC/ PC<sub>61</sub>BM/BCP/Ag.

#### 2.3. Characterization

The film surface morphology was characterized by scanning electron microscopy (SEM) using a field emission scanning electron microscope (LYR3 XMH, Tescan) and atomic force microscopy (AFM) in Peak-Force Tapping mode (Bruker Dimension Icon Atomic Force Microscope) in tapping mode. Surface potential mode was utilized to study the surface

potential of the films using Kelvin porbe force microscopy (KPFM). The X-ray diffractometry (XRD) diffraction patterns of perovskite films were collected by MiniFlex600 (Rigaku) with a 20 range from 5 to 45° under Cu K $\alpha$  radiation source  $\lambda = 1.54$  Å. Grazing-incidence wide-angle X-ray scattering (GIWAXS) results were also obtained to study crystallinity of perovskite films with an X-ray wavelength of 1.54 Å and incidence angle of 0.2° under vacuum conditions based on a laboratory beamline system (Xenocs Inc. Xeuss 2.0) with an X-ray wavelength of 1.54 Å and incidence angle of  $0.2^{\circ}$  under vacuum condition. The images of GIWAXS were recorded on a Pilatus 1 M detector (Dectris Inc.) and processed using Irena and Nika package in Igor software. Cary 60 UV-vis spectrophotometer (Agilent Technologies) was used to obtain the absorption spectra of perovskite film. The water contact angle measurement of the films was carried out using a contact angle goniometer (Ossila). The current-voltage (J-V) characteristic curves and sunlight stability of PSCs were collected by digital source meter (Keithley, 2400, USA) under the illumination AM1.5G (100 mW/cm<sup>2</sup>) using a G2V Pico solar simulator at a scan rate of 10 mV/s between 1.2 and 0 V. The steady-state photoluminescence (PL) spectra and the time-resolved photoluminescence (TRPL) spectra under 461 nm excitation wavelength of PSCs were obtained by the fluorescence spectrometer (FluoroMax, Horiba) with DeltaHub and NanoLED. The electrochemical workstation (CHI 604E) was applied to evaluate the series and recombination resistance of PSCs with a 0.9 V bias voltage in the dark condition. 5 mV AC voltage and swept from 1 Hz to 1 M Hz frequency were used for the electrochemical impedance spectroscopy (EIS) measurements. The external quantum efficiency (EQE) measurements were conducted using a quantum efficiency measurement system (IQE-200B, Newport). The J-V curves of electron-only and hole-only devices were collected by the source meter (Keithley, 2450, USA). XPS analysis was performed using a Thermo-Fisher ESCALAB Xi<sup>+</sup> spectrometer equipped with a monochromatic Al X-ray source (1486.6 eV, 300 mm<sup>2</sup> spot size). Measurements were performed using the standard magnetic lens mode and charge compensation. The base pressure in the analysis chamber during spectral acquisition was  $3 \times 10^{-7}$  mBar. Spectra were collected at a takeoff angle of 90° from the plane of the surface. The pass energy of the analyzer was set at 20 eV for high-resolution spectra and 150 eV for survey scans, with energy resolutions of 0.1 eV and 1.0 eV, respectively. Binding energies were calibrated with respect to C 1s at 285.3 eV. All spectra were recorded using the Thermo Scientific Avantage software; data files were translated to VGD format and processed using the Thermo Avantage package v5.9904. Sub-picosecond-to-nanosecond transient absorption (TA) data were collected by a home-built system powered by a Ti:sapphire pulse regenerated amplifier (Regen, Phidia-C, Uptek). Briefly, the 800 nm, 4 mJ, 150 fs pulses generated by the Regen with a repetition rate of 1 kHz were split to produce the pump and probe beams. About 2 mW of the 800 nm beam was introduced to an optical parametric amplifier (OPA-C, Light-Conversion), and the 2060 nm idler was picked up after the OPA to generate the 515 nm TA pump through fourth-Harmonic generation (FHG), by two beta barium borate (BBO) crystals. The residual IR light after FHG was removed using a serial of longpass (LP) dichromatic beam splitters. Specifically, a pair of 1080 nm LP beam splitters were employed after the first BBO crystal to remove the 2060 nm idler, and a pair of 505 nm LP beam splitters after the second BBO, to remove the 1030 nm residual. The pump beam was chopped to 500 Hz, attenuated to 8 or 12 nJ per pulse, and softly focused on the sample. The choice of the low pump fluence was controlled to keep the photoinduced bleach signal of MAPbI<sub>3</sub> in the linear regime (Fig. S1a). The TA system employed a mixture of H<sub>2</sub>O/D<sub>2</sub>O with a 1:1 ratio (v/v) as the medium to produce the broadband white-light continuum (WL) probe. A small portion of the 800 nm (~50 mW) Regen output was picked up before the OPA and bounced four times on a retroreflector mounted on a linear translation stage. This optical delay setup provided a time window up to 4200 ps. The 800 nm beam was then focused on the WL medium contained in a quartz cuvette with a path length of 5 mm. The liquid WL medium was agitatedly stirred to avoid overheating. The

resulting WL was then separated to two by a 70:30 beam splitter: the reflected beam was used to probe the sample, while the transmitted beam served as the reference to compensate for the pulse-to-pulse discrepancy. The sample and the reference beam were focused on the sample plane by two spherical mirrors, respectively. A 720 nm shortpass filter was used before the sample to remove most of the 800 nm fundamental. The sample beam was overlapped with the pump beam on the surface of the perovskite, and the reference beam was raised 2.3 cm above the sample. The diverged sample and reference beams were collimated and focused to the slit of the spectrometer (SpectralPro-300i, Acton) and separately dispersed to two vertically aligned photodiode arrays (1024 pixels, EB Stresing). TA signals were calculated pixel-bypixel using the formula  $\Delta OD = -\log((\frac{I_S}{I_R})_{pump-on}/(\frac{I_R}{I_S})_{pump-off})$ , where  $I_S$ and  $I_R$  were the intensities of the sample and reference pulses, respectively. The TA system was automated with a home-built LabView program. Perovskite films were spin-coated to quartz substrates. During the data collection, perovskite films were sealed in a quartz cuvette, which was vacuumed and refilled with dry N2 three times. The integration time is 2 s for every time-delay point, and the collections were repeated three times and averaged. We ensured the intact of films during experiments by observing that the TA spectra and kinetics of the three collections overlapped each other (Fig. S1b).

#### 3. Results and discussion

The structure of the FPC in IPA is illustrated in Fig. 1a. The long alkyl chains and -COOH groups on the FPC are used to passivate the perovskite films. Fig. 1 b and c show the photographs obtained from water contact angle measurements of the bare perovskite film (control perovskite film) and FPC perovskite film (perovskite film modified with FPC), respectively. The water contact angles of perovskite films without and with FPC are 25.4° and 70.5°, respectively. The water contact angle of the perovskite film with FPC is larger compared to the control perovskite film, indicating the hydrophobic properties of the film surface. It is well known that carboxyl groups are hydrophilic, while the long alkyl chains are hydrophobic. Therefore, it is possible that the long alkyl chains are exposed to the air, leading to the hydrophobic properties of the FPC perovskite films. The -COOH groups may be attached to the perovskite film surface to passivate perovskite films. Fig. 1d shows the mechanism diagram of the perovskite film passivation by FPC. We perform several characterization measurements to further evaluate the chemical interactions between perovskite films and FPC polymer. Fig. 1e exhibits the FTIR spectra of control perovskite film and FPC perovskite film. The bending vibration of C-H in the control perovskite film is located at 780 cm<sup>-1</sup>, and the peak shifts to 782 cm<sup>-1</sup> after FPC modification, which is explained by the environment change around perovskite caused by FPC passivation [42]. The local environment of the perovskite films is changed by the FPC passivation due to the interaction between perovskite film and FPC, resulting in the shift of bending vibration of C-H in the perovskite film. Besides, the bending vibrations of C-N of the perovskite films without and with FPC are located at 1141 cm<sup>-1</sup> and 1136 cm<sup>-1</sup>, respectively [43]. The shift of the FTIR peaks of the perovskite films caused by the FPC modification indicates the interactions between the FPC and the perovskite grains, leading to the changed environment of perovskite, which may influence the charge transport and performance of the devices.

XPS measurements are performed to further understand the chemical states of the elements at the surface of the perovskite films without and with FPC and to confirm the interaction between FPC and perovskite films. Fig. 1f shows the C 1s XPS spectra of the control perovskite films, FPC perovskite films, and FPC powder. The peaks at 285.3 eV are attributed to C–C bonds. The FPC powerds exhibits three components located at 285.3 eV, 287 eV and 289 eV, which are attributed to C–C, C–O/C–N, and COOH bonds, respectively [44]. The C–N/C–O and COOH peaks of perovskite with FPC are very similar to corresponding

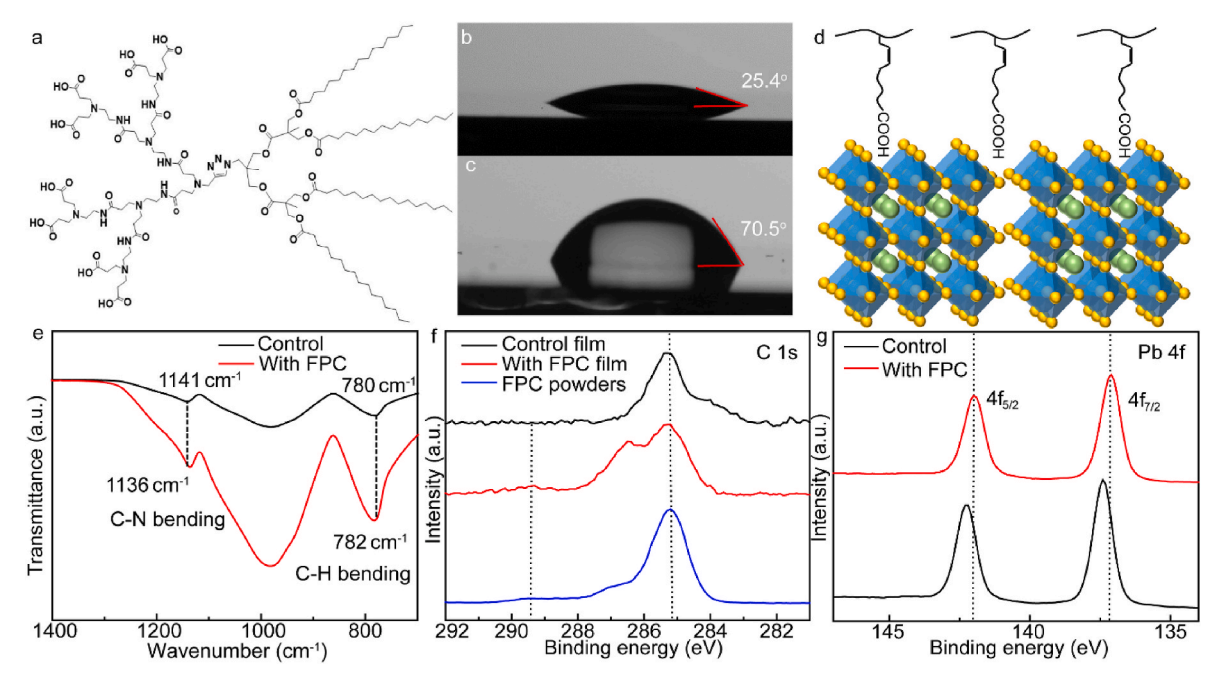
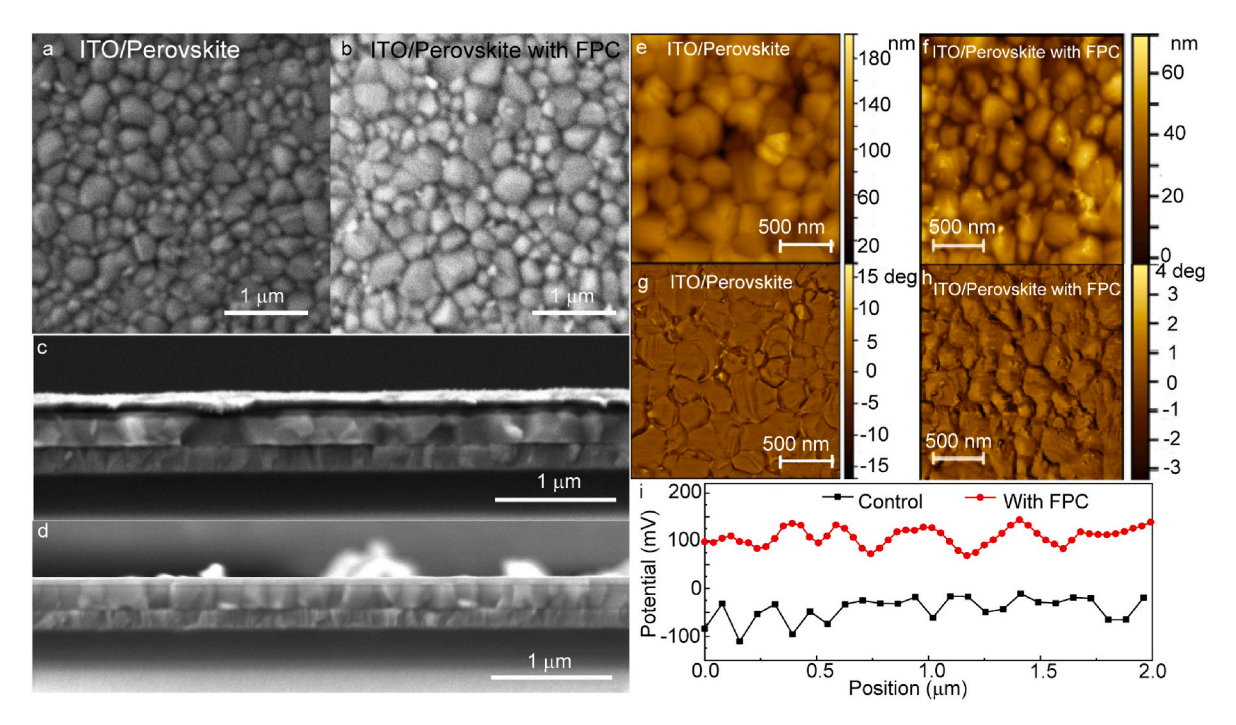


Fig. 1. a The structure of FPC; b-c The photographs of water contact angels of perovskite films without and with FPC; d The schematic of perovskite film passivated by FPC through –COOH groups; e the FTIR spectra of perovskite films with and without FPC; f C 1s XPS spectra of perovskite film, perovskite film with FPC, and FPC powders; g Pb 4f XPS spectra of perovskite films with and without FPC.

p0ositions of FPC powders, thus the C–N/C–O and COOH peaks of perovskite with FPC originate from FPC. The C 1s XPS results confirm that FPC is successfully introduced to the perovskite films. In addition, Fig. 1g exhibits the XPS spectra of Pb 4f for control and FPC perovskite films. Two main peaks are observed at 142.2 eV (Pb  $4f_{5/2}$ ) and 137.4 eV (Pb  $4f_{7/2}$ ) in the control perovskite film. For the FPC perovskite film, the two main peaks shift to 141.9 eV (Pb  $4f_{5/2}$ ) and 137.1 eV (Pb  $4f_{7/2}$ ), respectively. Compared to the control perovskite film, the two peaks of Pb 4f shift to the low binding energy side by FPC. This result confirms

the interactions between FPC and perovskite films, which is consistent with the FTIR results.

The morphology of the MAPbI $_3$  films plays an important role in terms of charge transport and device performance. SEM and AFM are used to investigate the morphology of the perovskite films influenced by FPC. Fig. 2a and b shows the top-view SEM images of control and FPC perovskite films (FPC concentration: 0.05 mg/mL), respectively. Two SEM images show similar morphology and MAPbI $_3$  grains with 100–300 nm are observed for both films. However, FPC perovskite film exhibits



**Fig. 2.** a-b top-view SEM images of perovskite films without and with FPC passivation; c-d The cross-section SEM images of perovskite films without and with FPC passivation; e-f AFM height images of perovskite films without and with FPC passivation; i The potential map of ITO/PTAA/Perovskite and ITO/PTAA/Perovskite/FPC films.

some smaller particles at the grain boundaries compared to the control film, which is consistent with the sizes of FPC (~100 nm) [41]. The FPC molecules may be located at the grain boundaries of the film. Fig. 2c and d shows the cross-sectional SEM images of devices without and with FPC (0.05 mg/mL). It is clear to see the layer-by-layer structure of the devices, and the MAPbI3 light-absorbing layer has good contact with the hole transport layer (HTL) and electron transport layer (ETL), benefiting charge transport in devices. The cross-sectional SEM images of the film with FPC exhibits more uniform structure, and the grain boundaries are not obvious compared to the control perovskite films, which is explained by the FPC passivation on the grains. Fig. 2e and f shows AFM height images of control and FPC perovskite films (0.05 mg/mL) on ITO substrates. We also check the phase images of perovskite without and with FPC passivation, as shown in Fig. 2g and h. Smaller particles are observed on the FPC perovskite film compared to the control perovskite film, which is attributed to the FPC particles. The root mean square (RMS) roughness of ITO/MAPbI3 film decreases from 17.8 nm to 10.5 nm after modification by FPC (Fig. 2e and f). Therefore, FPC modification improves the film flatness and the smoothness. The control film shows unmodified GBs in Fig. 2a, while the FPC may be distributed in GBs of perovskite films to modify the GBs of the perovskite films to improve the film flatness (Fig. 2b). The enhanced RMS indicates the improved interface connection of perovskite/PC61BM, which may reduce the interface resistance and enhance charge transport. Hence, FPC passivation enhances the charge transport, which is consistent to other literature reported [45,46]. Fig. 2i shows the contact potential differences (CPD) of the ITO/MAPbI3 and ITO/MAPbI3/FPC films obtained by KPFM. The average CPD values for the perovskite films with and without FPC are about +120 mV and -60 mV, respectively. The improvement of 180 mV is obtained by FPC, which is attributed to the arrangement of the FPC molecules on the perovskite film surface. This is very similar to the results of tetraoctylammonium bromide in OLED and OPV [47,48]. The charge transport in the devices can be facilitated by the increased CPD according to the literature, which also benefits the Voc of the devices [49,50].

To evaluate the effect of FPC passivation on the crystallinity and the light-harvesting ability of the perovskite films, the UV-vis absorption, XRD, and GIWAXS measurements are carried out. The UV-vis absorption spectra of the perovskite films with and without FPC passivation are shown in Fig. 3a. The peaks at  $\sim$ 750 nm are attributed to the perovskite film absorption. The peak of FPC perovskite film is slightly higher than the control perovskite film, indicating that the FPC passivation enhances the light-harvesting of perovskite films. Fig. 3b shows the XRD diffraction patterns of perovskite films with and without FPC passivation. The diffraction peak at 12.68° is attributed to PbI2, and the peaks of 14.08° and 28.42° are indexed to the (110) and (220) crystal planes of perovskite films, indicating the FPC polymer passivation does not affect the crystal structure of perovskite. Fig. 3c and d shows the GIWAXS rings of perovskite films without and with FPC (0.25 mg/mL), and Fig. S2 exhibits the GIWAXS diffraction rings of perovskite films with different FPC concentrations. There are two main rings at q = 1.0 and  $2.0 \text{ Å}^{-1}$ which are assigned to the perovskite crystal planes of (110) and (220). This further confirms that the introduction of FPC doesn't influence the crystal structures of the perovskite films.

In addition, to study the influence of FPC passivation on the performance of PSCs, the current density-voltage curves (J-V) of devices with different FPC concentrations are measured (Fig. S3). The average PCE of 17.5% is obtained for the control PSCs (No FPC). The average PCE increases from 17.9% to 18.7% as the FPC concentration increases from 0.15 mg/mL to 0.25 mg/mL. When the concentration of FPC achieves 0.5 mg/mL, the average PCE of PSCs decreases to 17%. Thus, 0.25 mg/mL is the optimal concentration of FPC to passivate PSCs. Fig. 4a and b shows the Voc and PCE values of PSCs with and without FPC based on 25 devices prepared with the same experimental conditions. It is clear to see that the PSCs with FPC exhibit higher Voc and PCE compared to the control PSCs. The average Voc value of PSCs increases from 1.06 V to 1.08 V, and the average PCE increases from 18.0% to 18.8% as FPC is utilized to passivate PSCs. Fig. 4c shows the champion PSCs with and without the FPC. The control PSC exhibits the PCE of 18.71%, Jsc of 23.23 mA/cm<sup>2</sup>, Voc of 1.06 V, and FF of 75.42%. PSC

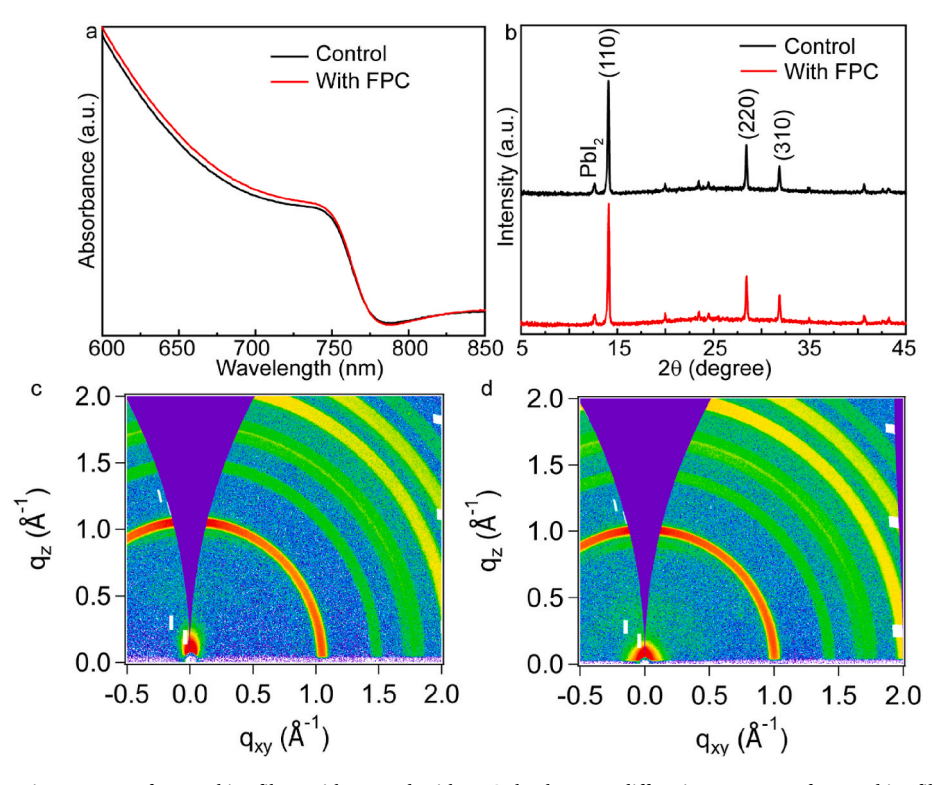


Fig. 3. a The UV-vis absorption spectra of perovskite films without and with FPC; b The XRD diffraction patterns of perovskite films without and with FPC passivation; c The GIWAXS patterns of control film; d The GIWAXS patterns of perovskite with FPC passivation (0.25 mg/mL).

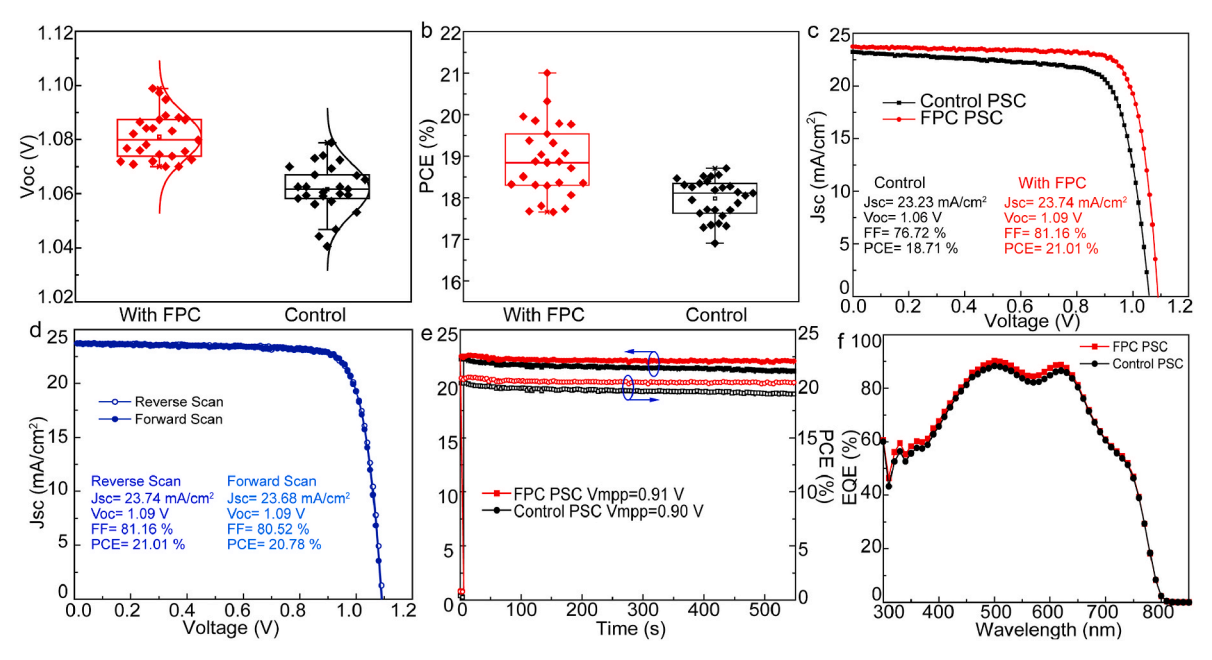


Fig. 4. a The Voc of PSCs with and without FPC passivation (0.25 mg/mL); b The PCE of PSCs with and without FPC passivation (0.25 mg/mL); c The J-V curves of champion devices with and without FPC passivation; d The J-V curves of PSCs with FPC passivation under different scan directions; e The light stability of PSCs with and without FPC passivation under Vmpp; f The EQE spectra of PSCs with and without FPC passivation.

with FPC shows the PCE of 21.01%, Jsc of 23.74 mA/cm², Voc of 1.09 V, and FF of 81.16%. The Jsc does not change that much. The enhancement of PCE and  $V_{\rm OC}$  is attributed to the passivation effect of FPC. The trap states and nonradiative recombination of the PSCs may be decreased by FPC passivation due to the interaction between FPC and perovskite, leading to improved Voc and PCE of the devices [51,52]. In addition, the performance of PSCs with FPC under forward and reverse scans are shown in Fig. 4d. The hysteresis index can be calculated by the following formula:

$$HI = \frac{PCE_R - PCE_F}{PCE_R}$$

where PCE $_R$  is the PCE under reverse scan and PCE $_F$  is the PCE under forward scan. Therefore, the HI value of PSCs modified by FPC is 0.011, which can be ignored compared to the control PSC (0.017). It is reported that the HI is related to the defects of the perovskite films [53]. Therefore, The small HI of the modified PSC indicates the decreased defects caused by FPC modification. Fig. 4e shows the PSCs with and without FPC under one sunlight soaking for 550 s. The current density of the control PSC decreases from 22.26 mA/cm $^2$  to 21.26 mA/cm $^2$ , keeping

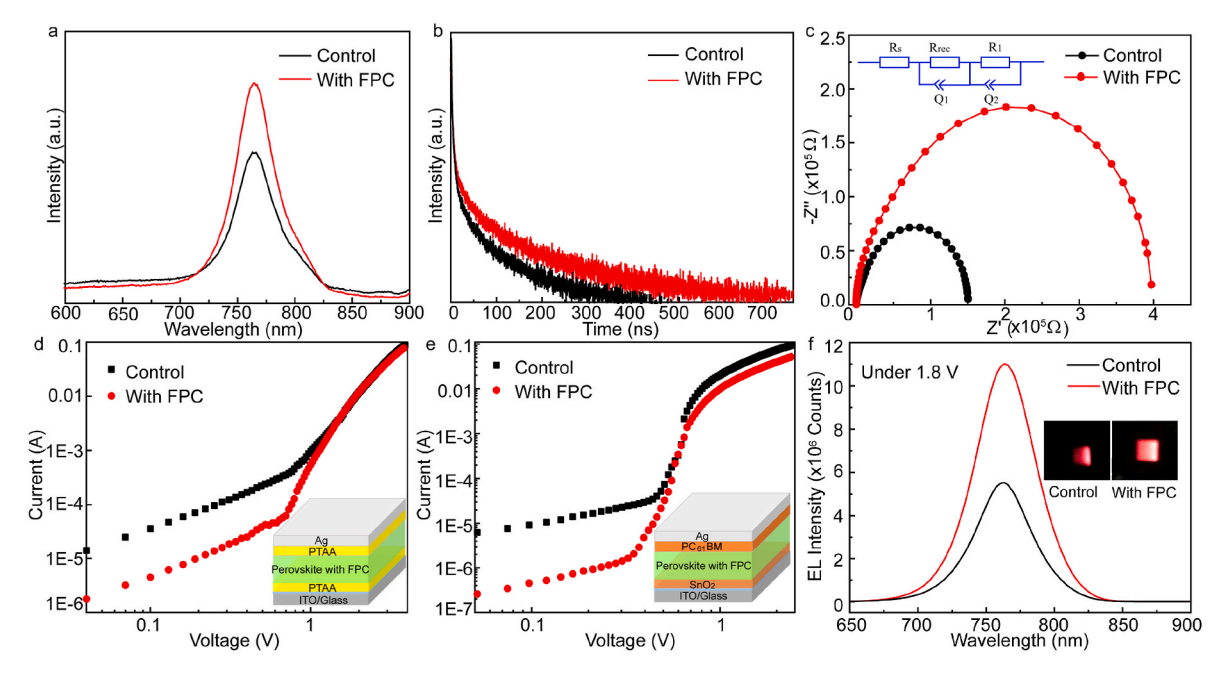


Fig. 5. a The PL spectra of perovskite films with and without FPC passivation; b The TRPL spectra of perovskite films with and without FPC passivation; c The Nyquist plot of the PSCs with and without FPC passivation; d The hole-only devices with and without FPC passivation; e The electron-only devices with and without FPC passivation; f The EL spectra of PSCs with and without FPC passivation under 1.8 V.

95.5% of its initial current density, and the PCE maintains 95.77% of the initial PCE value under the maximum power point (0.90 V). However, the PSC with FPC still keeps 99.0% of its initial current density and the PCE keeps 98.4% of its initial PCE after soaking for 550 s with the maximum power point (0.91 V). Thus, the control PSC shows a quicker decay than the PSC with FPC. We think the FPC passivation suppresses ion migration and reduces interfacial defects caused by light soaking according to the literature [54,55], which will be confirmed by the PL, TRPL, EIS, electron and hole only devices. Fig. 4f displays the EQE spectra of control and modified PSCs, and both of them have a photoresponse at 300–800 nm. The EQE of the control and the modified PSCs show very similar intensities. EQE intensity is correlated with the Jsc of the devices [56]. The Jsc of the modified and control devices show similar values (Fig. 4c). Therefore, it is reasonable to observe similar EQE intensities for the control and modified devices.

Furthermore, the influence of FPC passivation on charge recombination and extraction of PSCs are investigated by PL, TRPL, and electrical impedance spectroscopy (EIS) measurements. As shown in Fig. 5a, the PL spectrum of FPC modified perovskite film exhibits higher intensity than the control perovskite film, which suggests that the FPC passivation effectively reduces the nonradiative recombination. The TRPL spectra (Fig. 5b) show the lifetime of perovskite film with and without FPC, and it is clear that the perovskite film modified by FPC exhibits a longer lifetime than the control film. The lifetime curves of these two films are fitted by bi-exponential function, as illustrated in the following formula:

$$Y = A_1 \exp(\frac{-t}{\tau_1}) + A_2 \exp(\frac{-t}{\tau_2})$$

where  $A_1$  and  $A_2$  are the relative amplitudes;  $\tau_1$  and  $\tau_2$  are the values of the lifetime for the fast and slow decay, respectively. For the control perovskite film, the  $\tau_1$  is 43.8 ns and  $\tau_2$  175.5 ns. However, the lifetime values of perovskite film with FPC increase to 55.9 ns 223.9 ns for  $\tau_1$  and  $\tau_2$ , respectively. The fast decay is related to the surface defects of the films (surface component), and the slow decay is associated with the bulk defects, which reveals the decay process of excitons inside perovskite films [57,58]. Furthermore, the charge recombination is caused by defects including GBs and surface defects [17]. The lifetime of carriers in perovskite film for these two processes (fast and slow decay) is prolonged after FPC passivation, indicating decreased defect densities at the GBs and the interface, which suppresses the trap-assisted recombination in the devices. The EIS measurements are carried out with a bias of 0.9 V under dark conditions, and the results are illustrated in Fig. 5c. The Nyquist plot of the PSCs with and without FPC passivation are fitted by the equivalent circuit shown in the inset of Fig. 5c and the fitting parameters of series resistance (Rs) and recombination resistance (Rrec) are displayed in Table S1 [49]. Rs decreases from 18.55 to 9.63  $\Omega$  and the Rrec increases from  $1.42 \times 10^5$  to  $3.52 \times 10^5$   $\Omega$  as PSCs are modified by FPC, which is attributed to the reduced charge recombination by FPC passivation [61,62]. To investigate the trap density for the positive and negative defects in the PSCs, the hole-only and electron-only devices are fabricated. The J-V curves of the hole-only and electron-only devices are exhibited in Fig. 5d and e, respectively. The structure of the hole-only devices is ITO/PTAA/MAPbI<sub>3</sub>/PTAA/Ag, and the structure of electron-only devices is ITO/SnO<sub>2</sub>/MAPbI<sub>3</sub>/PC<sub>61</sub>M/Ag, which are shown in the insert Fig. 5d and e. The J-V curves of the hole-only and electron-only devices exhibit three behaviors, which are composed of an ohmic region (n = 1), a trap-filled limit (TFL) region (n > 3), and a space-charge limited current (SCLC) region (n = 2) [63,64]. The trap density  $(n_t)$  can be calculated by the following equation,

$$V_{TFL} = \frac{en_t L^2}{2\varepsilon\varepsilon_0}$$

where  $V_{TFL}$  is the onset voltage of hole or electron only devices in the TFL region; e is the elementary charge of an electron; L is the perovskite film

thickness;  $\varepsilon$  and  $\varepsilon_0$  are the relative dielectric constant of MAPbI<sub>3</sub> and vacuum dielectric constant, respectively. The calculated hole-trap density values of PSCs with and without FPC are  $3.85\times10^{16}\,\text{cm}^{-3}$  and 4.53 $imes 10^{16} \, \mathrm{cm}^{-3}$ , respectively. The electron-trap density values of PSCs with and without FPC are  $2.04 \times 10^{16} \text{ cm}^{-3}$  and  $2.66 \times 10^{16} \text{ cm}^{-3}$ , respectively. It is clear to see that both hole and electron trap densities of perovskite film decrease after FPC modification, which benefits charge transport and the device performance. The electroluminescence (EL) spectra are used to analyze the nonradiative recombination of PSCs. The EL intensity of PSCs with FPC passivation increases with the bias increasing as shown in Fig. S4. Besides, the peak of EL spectra is located at  $\sim$ 750 nm, which is consistent with the PL spectra (Fig. 5a). Fig. 5f shows the EL spectra of PSCs with and without FPC under 1.8 V bias. The EL intensity of PSC with FPC is almost twice as high as the control PSC. In addition, the photographs of electroluminescence of PSCs without and with FPC are shown in the inset of Fig. 5e. The EL intensity of PSC with FPC is brighter compared to the control PSC under a bias of 1.8 V, which indicates the reduction of charge recombination of PSCs by FPC passivation [65].

To further investigate the influence of FPC passivation on the interface charge transfer and recombination kinetics between the perovskite layer and PC<sub>61</sub>BM layer, we carry out transient absorption (TA) spectrum measurements. Fig. 6a and b shows the plots of TA spectra of the FPC modified perovskite films without and with PC<sub>61</sub>BM, and Fig. 6 c shows the kinetic traces for the bleach signal at 760 nm. With the presence of PC<sub>61</sub>BM, the perovskite bleach at 760 nm undergoes a small growth at the early time with a time constant of  $\sim$ 25 ps, likely due to the contribution of the PC<sub>61</sub>BM absorption to the carrier formation. The bleach then decays much faster contact to PC<sub>61</sub>BM, indicating that electrons generated in the perovskite layer are extracted by PC<sub>61</sub>BM [45]. Fitting the kinetic trace, we yield a rate constant of 0.43 ns<sup>-1</sup> for the decay of bleach in perovskite/FPC/PC<sub>61</sub>BM, and in the unmodified sample (perovskite/PC61BM), the bleach decays slightly faster (0.55 ns<sup>-1</sup>) than the modified sample. This result is expected given the insulate dendrimer layer likely increases the barrier for charge carriers to migrate across the interface. Compared to the long intrinsic lifetimes of charge carriers in perovskite measured by TR-PL (43.8 ns and  $\tau_2$  175.5 ns for the original sample, and 55.9 ns 223.9 ns for the FPC-modified sample), the charge transfer process, as measured by TA, in both modified and unmodified films are fast enough to guarantee efficient carrier extraction. The relatively small difference in charge transfer rates may not significantly affect the yield of charge separation at the interface between perovskite and PC<sub>61</sub>BM. Therefore, we speculate that the FPC layer enhances the device efficiency by retarding the detrimental trap-assisted charge recombination process at the interface after charge separation, and FPC effectively eliminates the surface traps [45,46].

To study the FPC passivation effects on the moisture and air stability of PSCs, the PSCs are exposed under 60  $\pm$  5% relative humidity (RH) and 25  $\pm$  5% RH conditions in the air. Fig. 7a shows devices with and without FPC exposed under  $60 \pm 5\%$  RH for 3500 min. The PSC with FPC keeps ~90% of the initial PCE. However, the control device maintains only ~50% of the original value. This result indicates FPC passivation protects device degradation from moisture and improves the moisture stability of PSCs. The long alkyl chains on FPC are hydrophobic (Fig. 1b and c) [66,67], leading to improved moisture stability of PSCs. Furthermore, the stability of PSCs under humidity 25  $\pm$  5% RH condition (30  $\pm$  5 °C) is illustrated in Fig. 7b. The device with FPC maintain  $\sim$ 82% of the initial PCE value for 30 days and the PCE of control PSC decreased to  $\sim$ 47% of the initial values. The device degradation is understood by the ion migration at the interface between the electron transport layer and the perovskite layer [68,69]. The improved stability is attributed to the stable interface caused by FPC passivation due to the strong interaction between the FPC and perovskite film, leading to improved air stability of the PSCs.

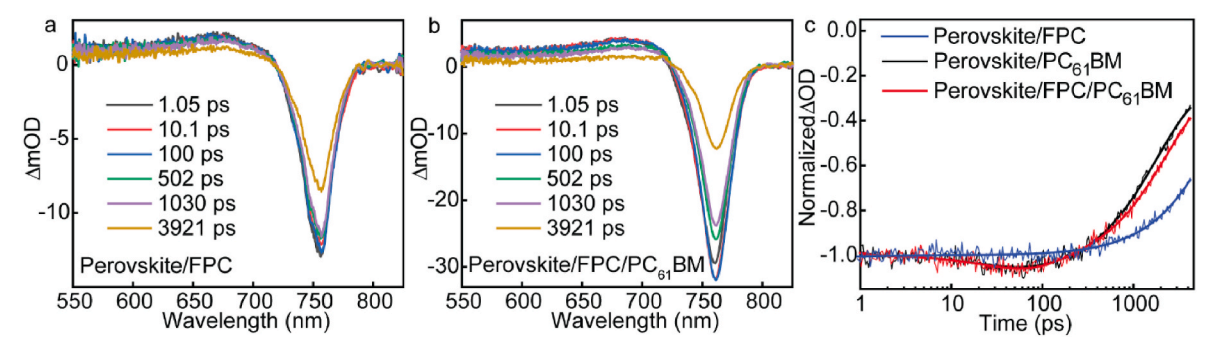


Fig. 6. a-b TA spectra of FPC-modified perovskite films without and with  $PC_{61}BM$  deposited on quartz substrates; c Normalized kinetic traces of the  $\sim$ 760 nm bleach signals of perovskite/FPC, perovskite/FPC, perovskite/FPC/PC<sub>61</sub>BM.

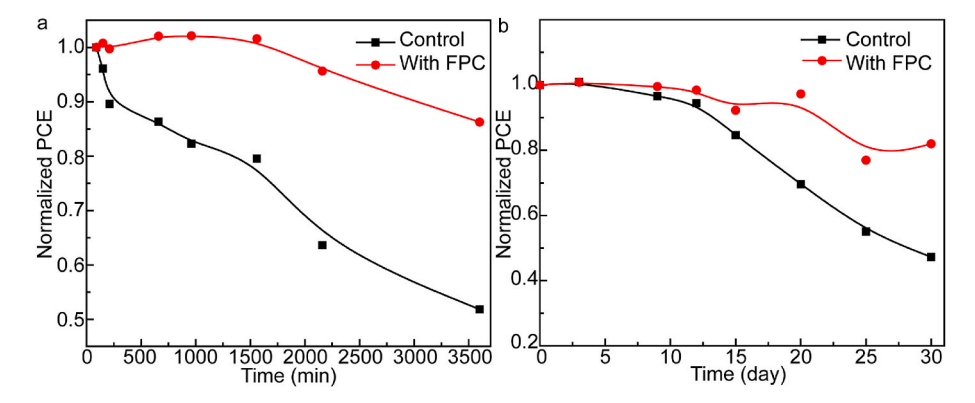


Fig. 7. a The stability of PSCs with and without FPC passivation under RH =  $60 \pm 5\%$ ; b The stability of PSCs with and without FPC passivation in the air (RH = 25%).

#### 4. Conclusions

In summary, we design a polymer with hydrophobic long alkyl chains and hydrophilic -COOH. The feasibility of applying -COOH functional group to passivate perovskite films to considerably increase device efficiency and using hydrophobic long alkyl chains to protect the devices from moisture by one material is demonstrated. The XPS and FTIR results show that the FPC has strong interaction with perovskite films. Thus, this is an effective strategy to modify defects in the perovskite films using our designed material. The hole-only devices and electron-only devices show that the trap-state densities greatly decrease. Furthermore, the FPC passivation decreases carrier recombination and improves charge transport. The PSCs with FPC passivation exhibit the PCE of 21.01% with Jsc of 23.74 mA/cm<sup>2</sup>, Voc of 1.09 V, and FF of 81.16%, which is higher than the control devices. In addition, the devices with FPC show much better stability in the moisture environment. The PSC with FPC passivation keeps ~90% of the initial PCE for 3500 min under  $60 \pm 5\%$  (RH). Also, the device with FPC could keep  $\sim 82\%$  of the initial PCE value under 25  $\pm$  5% and 30  $\pm$  5 °C for 30 days. Therefore, we believe this work could open a new paradigm for designing new organic materials with desired functional groups toward high-performance PSCs.

## CRediT authorship contribution statement

Yifang Qi: carried out device fabrication and characterization and wrote the original draft. Mahesh Loku Yaddehige: synthesized the polymer. Kevin A. Green: did the AFM measurement. Jaiden Moore: did the TRPL measurement. Surabhi Jha: did the XPS measurement. Guorong Ma: carried out the GIWAXS measurement. Chen Wang: did the ultrafast spectra measurement. Davita L. Watkins: synthesized the polymer. Xiaodan Gu: carried out the GIWAXS measurement. Derek

**Patton:** did the XPS measurement. **Sarah E. Morgan:** did the AFM measurement. **Qilin Dai:** surprised the project and edit the manuscript. All the authors approved the final manuscript.

# Declaration of competing interest

The authors declare that they have no known competing financial interests or personal relationships that could have appeared to influence the work reported in this paper.

#### Acknowledgment

This material is based on work supported by the National Science Foundation under Grant No. 1757220. The steady-state PL and TRPL equipment used in this work is supported by National Science Foundation Research Initiation Award: Novel Perovskite Solar Cells Based on Interface Manipulation (Award#1900047). XPS instrumentation used in this work was supported by the NSF Major Research Instrumentation Program (DMR-1726901).

# Appendix A. Supplementary data

Supplementary data to this article can be found online at https://doi.org/10.1016/j.jpowsour.2022.231518.

## References

- L. Gil-Escrig, C. Dreessen, F. Palazon, Z. Hawash, E. Moons, S. Albrecht, M. Sessolo, H.J. Bolink, Efficient wide-bandgap mixed-cation and mixed-halide perovskite solar cells by vacuum deposition, ACS Energy Lett. 6 (2021) 827–836, https://doi. org/10.1021/acsenergylett.0r02445.
- [2] J. Chen, N.-G. Park, Materials and methods for interface engineering toward stable and efficient perovskite solar cells, ACS Energy Lett. 5 (2020) 2742–2786, https:// doi.org/10.1021/acsenergylett.0c01240.

- [3] H. Sun, K. Deng, J. Xiong, L. Li, Graded bandgap perovskite with intrinsic n-p homojunction expands photon harvesting range and enables all transport layer-free perovskite solar cells, Adv. Energy Mater. 10 (2020), 1903347, https://doi.org/ 10.1002/aenm.201903347.
- [4] K. Minjin, J. Jaeki, L. Haizhou, L.T. Kyung, E.F. T, L. Yuhang, C.I. Woo, C.S. Ju, J. Yimhyun, K. Hak-Beom, M. Sung-In, K. Young-Ki, L. Heunjeong, A.N. Gyeong, C. Shinuk, T.W. R, Z.S. M, H. Anders, K.J. Young, G. Michael, K.D. Suk, Conformal quantum dot–SnO2 layers as electron transporters for efficient perovskite solar cells, Science 375 (2022) 302–306, https://doi.org/10.1126/science.abh1885, 80-.
- [5] C.-G. Wu, C.-H. Chiang, Z.-L. Tseng, M.K. Nazeeruddin, A. Hagfeldt, M. Grätzel, High efficiency stable inverted perovskite solar cells without current hysteresis, Energy Environ. Sci. 8 (2015) 2725–2733, https://doi.org/10.1039/c5ee00645g.
- [6] Z. Wang, L. Zeng, C. Zhang, Y. Lu, S. Qiu, C. Wang, C. Liu, L. Pan, S. Wu, J. Hu, G. Liang, P. Fan, H. Egelhaaf, C.J. Brabec, F. Guo, Y. Mai, Rational interface design and morphology control for blade-coating efficient flexible perovskite solar cells with a record fill factor of 81%, Adv. Funct. Mater. 30 (2020), 2001240 https://doi.org/10.1002/adfm.202001240.
- [7] Y.Y. Kim, T.-Y. Yang, R. Suhonen, A. Kemppainen, K. Hwang, N.J. Jeon, J. Seo, Roll-to-roll gravure-printed flexible perovskite solar cells using eco-friendly antisolvent bathing with wide processing window, Nat. Commun. 11 (2020), https://doi.org/10.1038/s41467-020-18940-5.
- [8] V. Babu, R. Fuentes Pineda, T. Ahmad, A.O. Alvarez, L.A. Castriotta, A. Di Carlo, F. Fabregat-Santiago, K. Wojciechowski, Improved stability of inverted and flexible perovskite solar cells with carbon electrode, ACS Appl. Energy Mater. 3 (2020) 5126–5134, https://doi.org/10.1021/acsaem.0c00702.
- [9] X. Meng, Z. Cai, Y. Zhang, X. Hu, Z. Xing, Z. Huang, Z. Huang, Y. Cui, T. Hu, M. Su, X. Liao, L. Zhang, F. Wang, Y. Song, Y. Chen, Bio-inspired vertebral design for scalable and flexible perovskite solar cells, Nat. Commun. 11 (2020), https://doi.org/10.1038/s41467-020-16831-3.
- [10] F. Li, X. Deng, F. Qi, Z. Li, D. Liu, D. Shen, M. Qin, S. Wu, F. Lin, S.-H. Jang, J. Zhang, X. Lu, D. Lei, C.-S. Lee, Z. Zhu, A.K.-Y. Jen, Regulating surface termination for efficient inverted perovskite solar cells with greater than 23% efficiency, J. Am. Chem. Soc. 142 (2020) 20134–20142, https://doi.org/10.1021/jacs.0c09845.
- [11] T.-H. Han, J.-W. Lee, C. Choi, S. Tan, C. Lee, Y. Zhao, Z. Dai, N. De Marco, S.-J. Lee, S.-H. Bae, Y. Yuan, H.M. Lee, Y. Huang, Y. Yang, Perovskite-polymer composite cross-linker approach for highly-stable and efficient perovskite solar cells, Nat. Commun. 10 (2019), https://doi.org/10.1038/s41467-019-08455-z.
- [12] A. Castro-Méndez, J. Hidalgo, J. Correa-Baena, The role of grain boundaries in perovskite solar cells, Adv. Energy Mater. 9 (2019), 1901489, https://doi.org/ 10.1002/aenm.201901489.
- [13] F. Gao, Y. Zhao, X. Zhang, J. You, Recent progresses on defect passivation toward efficient perovskite solar cells, Adv. Energy Mater. 10 (2019), 1902650, https://doi.org/10.1002/aenm.201902650.
- [14] S. Yuan, Y. Cai, S. Yang, H. Zhao, F. Qian, Y. Han, J. Sun, Z. Liu, S. (Frank) Liu, Simultaneous cesium and acetate coalloying improves efficiency and stability of FA 0.85 MA 0.15 Pbl 3 perovskite solar cell with an efficiency of 21.95%, Sol. RRL. 3 (2019) 1900220 https://doi.org/10.1002/cpl/201900220
- (2019), 1900220 https://doi.org/10.1002/solr.201900220.
  [15] Y. Lin, L. Shen, J. Dai, Y. Deng, Y. Wu, Y. Bai, X. Zheng, J. Wang, Y. Fang, H. Wei, W. Ma, X.C. Zeng, X. Zhan, J. Huang, π-Conjugated Lewis base: efficient trappassivation and charge-extraction for hybrid perovskite solar cells, Adv. Mater. 29 (2016), 1604545, https://doi.org/10.1002/adma.201604545.
- [16] K.K. Wong, A. Fakharuddin, P. Ehrenreich, T. Deckert, M. Abdi-Jalebi, R.H. Friend, L. Schmidt-Mende, Interface-dependent radiative and nonradiative recombination in perovskite solar cells, J. Phys. Chem. C 122 (2018) 10691–10698, https://doi. org/10.1021/acs.ipcc.8b00998.
- [17] T.S. Sherkar, C. Momblona, L. Gil-Escrig, J. Ávila, M. Sessolo, H.J. Bolink, L.J. A. Koster, Recombination in perovskite solar cells: significance of grain boundaries, interface traps, and defect ions, ACS Energy Lett. 2 (2017) 1214–1222, https://doi.org/10.1021/acsenergylett.7b00236.
- [18] Z. Wu, M. Jiang, Z. Liu, A. Jamshaid, L.K. Ono, Y. Qi, Highly efficient perovskite solar cells enabled by multiple ligand passivation, Adv. Energy Mater. 10 (2020), 1903696, https://doi.org/10.1002/aenm.201903696.
- [19] X. Hu, H. Wang, M. Wang, Z. Zang, Interfacial defects passivation using fullerenepolymer mixing layer for planar-structure perovskite solar cells with negligible hysteresis, Sol. Energy 206 (2020) 816–825, https://doi.org/10.1016/j. solener.2020.06.057.
- [20] H. Li, J. Shi, J. Deng, Z. Chen, Y. Li, W. Zhao, J. Wu, H. Wu, Y. Luo, D. Li, Q. Meng, Intermolecular π–π conjugation self-assembly to stabilize surface passivation of highly efficient perovskite solar cells, Adv. Mater. 32 (2020), 1907396, https://doi. org/10.1002/adma.201907396.
- [21] S. Wang, A. Wang, X. Deng, L. Xie, A. Xiao, C. Li, Y. Xiang, T. Li, L. Ding, F. Hao, Lewis acid/base approach for efficacious defect passivation in perovskite solar cells, J. Mater. Chem. A. 8 (2020) 12201–12225, https://doi.org/10.1039/ d0ta03957h.
- [22] S. Akin, N. Arora, S.M. Zakeeruddin, M. Grätzel, R.H. Friend, M.I. Dar, New strategies for defect passivation in high-efficiency perovskite solar cells, Adv. Energy Mater. 10 (2019), 1903090, https://doi.org/10.1002/aenm.201903090
- [23] K. Cao, Y. Huang, M. Ge, F. Huang, W. Shi, Y. Wu, Y. Cheng, J. Qian, L. Liu, S. Chen, Durable defect passivation of the grain surface in perovskite solar cells with π-conjugated sulfamic acid additives, ACS Appl. Mater. Interfaces 13 (2021) 26013–26022, https://doi.org/10.1021/acsami.1c04601.
- [24] W. Zhang, X. Liu, B. He, Z. Gong, J. Zhu, Y. Ding, H. Chen, Q. Tang, Interface engineering of imidazolium ionic liquids toward efficient and stable CsPbBr3 perovskite solar cells, ACS Appl. Mater. Interfaces 12 (2020) 4540–4548, https:// doi.org/10.1021/acsami.9b20831.

- [25] S. Ghosh, T. Singh, Role of ionic liquids in organic-inorganic metal halide perovskite solar cells efficiency and stability, Nano Energy 63 (2019), 103828, https://doi.org/10.1016/j.nanoen.2019.06.024.
- [26] J. Peng, Y. Wu, W. Ye, D.A. Jacobs, H. Shen, X. Fu, Y. Wan, T. Duong, N. Wu, C. Barugkin, H.T. Nguyen, D. Zhong, J. Li, T. Lu, Y. Liu, M.N. Lockrey, K.J. Weber, K.R. Catchpole, T.P. White, Interface passivation using ultrathin polymer-fullerene films for high-efficiency perovskite solar cells with negligible hysteresis, Energy Environ. Sci. 10 (2017) 1792–1800, https://doi.org/10.1039/c7ee01096f.
- [27] X. Zheng, B. Chen, J. Dai, Y. Fang, Y. Bai, Y. Lin, H. Wei, X.C. Zeng, J. Huang, Defect passivation in hybrid perovskite solar cells using quaternary ammonium halide anions and cations, Nat. Energy 2 (2017), https://doi.org/10.1038/ penergy 2017 102
- [28] W. Qi, J. Li, Y. Li, K. Sohail, H. Ling, P. Wang, S. Jiao, F. Liu, X. Zhou, H. Wang, D. Zhang, Y. Ding, X. Chen, G. Hou, J. Luo, Y. Zhao, Y. Li, X. Zhang, Manipulated crystallization and passivated defects for efficient perovskite solar cells via addition of ammonium iodide, ACS Appl. Mater. Interfaces 13 (2021) 34053–34063, https://doi.org/10.1021/acsami.1c05903.
- [29] S. Qiu, X. Xu, L. Zeng, Z. Wang, Y. Chen, C. Zhang, C. Li, J. Hu, T. Shi, Y. Mai, F. Guo, Biopolymer passivation for high-performance perovskite solar cells by blade coating, J. Energy Chem. 54 (2021) 45–52, https://doi.org/10.1016/j.iechem.2020.05.040.
- [30] W. Chen, Y. Wang, G. Pang, C.W. Koh, A.B. Djurišić, Y. Wu, B. Tu, F. Liu, R. Chen, H.Y. Woo, X. Guo, Z. He, Conjugated polymer–assisted grain boundary passivation for efficient inverted planar perovskite solar cells, Adv. Funct. Mater. (2019), 1808855, https://doi.org/10.1002/adfm.201808855.
- [31] C.-Y. Chang, C.-C. Wang, Enhanced stability and performance of air-processed perovskite solar cells via defect passivation with a thiazole-bridged diketopyrrolopyrrole-based π-conjugated polymer, J. Mater. Chem. A. 8 (2020) 8593–8604, https://doi.org/10.1039/d0ta00978d.
- [32] Z. Xiao, Y. Yuan, Q. Wang, Y. Shao, Y. Bai, Y. Deng, Q. Dong, M. Hu, C. Bi, J. Huang, Thin-film semiconductor perspective of organometal trihalide perovskite materials for high-efficiency solar cells, Mater. Sci. Eng. R Rep. 101 (2016) 1–38, https://doi.org/10.1016/j.mser.2015.12.002.
- [33] R. Garai, R.K. Gupta, A.S. Tanwar, M. Hossain, P.K. Iyer, Conjugated polyelectrolyte-passivated stable perovskite solar cells for efficiency beyond 20, Chem. Mater. 33 (2021) 5709–5717, https://doi.org/10.1021/acs. chemmater.1c01436.
- [34] K. Xiao, Q. Han, Y. Gao, S. Gu, X. Luo, R. Lin, J. Zhu, J. Xu, H. Tan, Simultaneously enhanced moisture tolerance and defect passivation of perovskite solar cells with cross-linked grain encapsulation, J. Energy Chem. 56 (2021) 455–462, https://doi. org/10.1016/j.jechem.2020.08.020.
- [35] C. Ma, N.-G. Park, Paradoxical approach with a hydrophilic passivation layer for moisture-stable, 23% efficient perovskite solar cells, ACS Energy Lett. 5 (2020) 3268–3275, https://doi.org/10.1021/acsenergylett.0c01848.
- [36] X. Li, C.-C. Chen, M. Cai, X. Hua, F. Xie, X. Liu, J. Hua, Y.-T. Long, H. Tian, L. Han, Efficient passivation of hybrid perovskite solar cells using organic dyes with □COOH functional group, Adv. Energy Mater. 8 (2018), 1800715, https://doi.org/ 10.1002/aepm.201800715
- [37] P. Chen, X. Yin, W.-H. Chen, L. Song, P. Du, Y. Huang, N. Li, J. Xiong, Perovskite solar cells with PCE over 19% fabricated under air environment by using a dye molecule additive, Sustain. Energy Fuels 5 (2021) 2266–2272, https://doi.org/ 10.1039/d1se00013f.
- [38] M.E. Kayesh, K. Matsuishi, R. Kaneko, S. Kazaoui, J.-J. Lee, T. Noda, A. Islam, Coadditive engineering with 5-ammonium valeric acid iodide for efficient and stable Sn perovskite solar cells, ACS Energy Lett. 4 (2018) 278–284, https://doi. org/10.1021/acsenergylett.8b02216.
- [39] W. Zhang, L. He, D. Tang, X. Li, Surfactant sodium dodecyl benzene sulfonate improves the efficiency and stability of air-processed perovskite solar cells with negligible hysteresis, Sol. RRL. 4 (2020), 2000376, https://doi.org/10.1002/ solr.202000376
- [40] Y. Guo, X. Li, L. Kang, C. Cheng, X. He, X. Liu, J. Liu, Y. Li, C. Dong, Mechanistic understanding of cetyltrimethylammonium bromide-assisted durable CH3NH3PbI3 film for stable ZnO-based perovskite solar cells, ACS Appl. Energy Mater. 3 (2020) 9856–9865, https://doi.org/10.1021/acsaem.0c01571.
- [41] M.L. Yaddehige, I. Chandrasiri, A. Barker, A.K. Kotha, J.S. Dal Williams, B. Simms, P. Kucheryavy, D.G. Abebe, M.B. Chougule, D.L. Watkins, Structural and surface properties of polyamidoamine (PAMAM) – fatty acid-based nanoaggregates derived from self-assembling Janus dendrimers, ChemNanoMat 6 (2020) 1833–1842, https://doi.org/10.1002/cnma.202000498.
- [42] X. Wu, Y. Jiang, C. Chen, J. Guo, X. Kong, Y. Feng, S. Wu, X. Gao, X. Lu, Q. Wang, G. Zhou, Y. Chen, J. Liu, K. Kempa, J. Gao, Stable triple cation perovskite precursor for highly efficient perovskite solar cells enabled by interaction with 18C6 stabilizer, Adv. Funct. Mater. 30 (2019), 1908613, https://doi.org/10.1002/adfm.201908613.
- [43] B. Li, Y. Zhang, L. Fu, T. Yu, S. Zhou, L. Zhang, L. Yin, Surface passivation engineering strategy to fully-inorganic cubic CsPbI3 perovskites for highperformance solar cells, Nat. Commun. 9 (2018), https://doi.org/10.1038/s41467-018-03169-0.
- [44] X. Chen, X. Wang, D. Fang, A review on C1s XPS-spectra for some kinds of carbon materials, Fullerenes, Nanotub. Carbon Nanostruct. 28 (2020) 1048–1058, https:// doi.org/10.1080/1536383x.2020.1794851.
- [45] X. Liu, Z. Yu, T. Wang, K.L. Chiu, F. Lin, H. Gong, L. Ding, Y. Cheng, Full defects passivation enables 21% efficiency perovskite solar cells operating in air, Adv. Energy Mater. 10 (2020), 2001958, https://doi.org/10.1002/aenm.202001958.
- [46] D.-Y. Son, J.-W. Lee, Y.J. Choi, I.-H. Jang, S. Lee, P.J. Yoo, H. Shin, N. Ahn, M. Choi, D. Kim, N.-G. Park, Self-formed grain boundary healing layer for highly

- efficient CH3NH3PbI3 perovskite solar cells, Nat. Energy 1 (2016), https://doi.org/10.1038/nenergy.2016.81.
- [47] C.-H. Wu, C.-Y. Chin, T.-Y. Chen, S.-N. Hsieh, C.-H. Lee, T.-F. Guo, A.K.-Y. Jen, T.-C. Wen, Enhanced performance of polymer solar cells using solution-processed tetra-n-alkyl ammonium bromides as electron extraction layers, J. Mater. Chem. A. 1 (2013) 2582, https://doi.org/10.1039/c2ta00975g.
- [48] S.-N. Hsieh, S.-W. Hsiao, T.-Y. Chen, C.-Y. Li, C.-H. Lee, T.-F. Guo, Y.-J. Hsu, T.-L. Lin, Y. Wei, T.-C. Wen, Self-assembled tetraoctylammonium bromide as an electron-injection layer for cathode-independent high-efficiency polymer light-emitting diodes, J. Mater. Chem. 21 (2011) 8715, https://doi.org/10.1039/clim00045d.
- [49] W. Yang, R. Su, D. Luo, Q. Hu, F. Zhang, Z. Xu, Z. Wang, J. Tang, Z. Lv, X. Yang, Y. Tu, W. Zhang, H. Zhong, Q. Gong, T.P. Russell, R. Zhu, Surface modification induced by perovskite quantum dots for triple-cation perovskite solar cells, Nano Energy 67 (2020), 104189, https://doi.org/10.1016/j.nanoen.2019.104189.
- [50] J. Xiong, Z. Dai, S. Zhan, X. Zhang, X. Xue, W. Liu, Z. Zhang, Y. Huang, Q. Dai, J. Zhang, Multifunctional passivation strategy based on tetraoctylammonium bromide for efficient inverted perovskite solar cells, Nano Energy 84 (2021), 105882, https://doi.org/10.1016/j.nanoen.2021.105882.
- [51] S.-C. Chen, D. Wang, Q. Zheng, Surface passivation of all-inorganic CsPbI 2 Br with a fluorinated organic ammonium salt for perovskite solar cells with efficiencies over 16%, Sol. RRL. 4 (2020), 2000321 https://doi.org/10.1002/solr.202000321.
- [52] Z. Xu, S.H. Teo, L. Gao, Z. Guo, Y. Kamata, S. Hayase, T. Ma, La-doped SnO2 as ETL for efficient planar-structure hybrid perovskite solar cells, Org. Electron. 73 (2019) 62–68, https://doi.org/10.1016/j.orgel.2019.03.053.
- [53] J.-W. Lee, S.-G. Kim, S.-H. Bae, D.-K. Lee, O. Lin, Y. Yang, N.-G. Park, The interplay between trap density and hysteresis in planar heterojunction perovskite solar cells, Nano Lett. 17 (2017) 4270–4276, https://doi.org/10.1021/acs.nanolett.7b01211.
- [54] J. Huang, H. Yan, D. Zhou, J. Zhang, S. Deng, P. Xu, R. Chen, H.-S. Kwok, G. Li, Introducing ion migration and light-induced secondary ion redistribution for phase-stable and high-efficiency inorganic perovskite solar cells, ACS Appl. Mater. Interfaces 12 (2020) 40364–40371, https://doi.org/10.1021/acsami.0c12068.
- [55] D. Lin, T. Shi, H. Xie, F. Wan, X. Ren, K. Liu, Y. Zhao, L. Ke, Y. Lin, Y. Gao, X. Xu, W. Xie, P. Liu, Y. Yuan, Ion migration accelerated reaction between oxygen and metal halide perovskites in light and its suppression by cesium incorporation, Adv. Energy Mater. 11 (2021), 2002552, https://doi.org/10.1002/aenm.202002552.
- [56] M.A. Cuiffo, J. Snyder, A.M. Elliott, N. Romero, S. Kannan, G.P. Halada, Impact of the fused deposition (FDM) printing process on polylactic acid (PLA) chemistry and structure, Appl. Sci. 7 (2017), https://doi.org/10.3390/app7060579.
- [57] J. Jiang, X. Sun, X. Chen, B. Wang, Z. Chen, Y. Hu, Y. Guo, L. Zhang, Y. Ma, L. Gao, F. Zheng, L. Jin, M. Chen, Z. Ma, Y. Zhou, N.P. Padture, K. Beach, H. Terrones, Y. Shi, D. Gall, T.-M. Lu, E. Wertz, J. Feng, J. Shi, Carrier lifetime enhancement in

- halide perovskite via remote epitaxy, Nat. Commun. 10 (2019), https://doi.org/10.1038/s41467-019-12056-1.
- [58] S. Dong, A. Valerio, C. Riccardo, Y. Mingjian, A. Erkki, B. Andrei, C. Yin, H. Sjoerd, R. Alexander, K. Khabiboulakh, L. Yaroslav, Z. Xin, D.P. A, M.O. F, S.E. H, B.O. M, Low trap-state density and long carrier diffusion in organolead trihalide perovskite single crystals, Science 347 (2015) 519–522, https://doi.org/10.1126/science. aaa2725. 80-.
- [61] Q. Zhou, Y. Gao, C. Cai, Z. Zhang, J. Xu, Z. Yuan, P. Gao, Dually-passivated perovskite solar cells with reduced voltage loss and increased super oxide resistance, Angew. Chem. 133 (2021) 8384–8393, https://doi.org/10.1002/ ange 202017148
- [62] M. Liu, Y. Xu, Z. Gao, C. Zhang, J. Yu, J. Wang, X. Ma, H. Hu, H. Yin, F. Zhang, B. Man, Q. Sun, Natural biomaterial sarcosine as an interfacial layer enables inverted organic solar cells to exhibit over 16.4% efficiency, Nanoscale 13 (2021) 11128–11137, https://doi.org/10.1039/d0nr09090e.
- [63] M. Sajedi Alvar, P.W.M. Blom, G.-J.A.H. Wetzelaer, Space-charge-limited electron and hole currents in hybrid organic-inorganic perovskites, Nat. Commun. 11 (2020), https://doi.org/10.1038/s41467-020-17868-0.
- [64] E.A. Duijnstee, J.M. Ball, V.M. Le Corre, L.J.A. Koster, H.J. Snaith, J. Lim, Toward understanding space-charge limited current measurements on metal halide perovskites, ACS Energy Lett. 5 (2020) 376–384, https://doi.org/10.1021/ acsenergylett.9b02720.
- [65] S. Kang, R. Jillella, J. Jeong, Y.-I. Park, Y.-J. Pu, J. Park, Improved electroluminescence performance of perovskite light-emitting diodes by a new hole transporting polymer based on the benzocarbazole moiety, ACS Appl. Mater. Interfaces 12 (2020) 51756–51765, https://doi.org/10.1021/acsami.0c16593.
- [66] Y. Gong, J. Shen, Y. Zhu, W. Yan, J. Zhu, L. Hou, D. Xie, C. Li, Tailoring charge transfer in perovskite quantum dots/black phosphorus nanosheets photocatalyst via aromatic molecules, Appl. Surf. Sci. 545 (2021), 149012, https://doi.org/ 10.1016/j.apsusc.2021.149012.
- [67] D. Jia, J. Chen, M. Yu, J. Liu, E.M.J. Johansson, A. Hagfeldt, X. Zhang, Dual passivation of CsPb1 3 perovskite nanocrystals with amino acid ligands for efficient quantum dot solar cells, Small 16 (2020), 2001772, https://doi.org/10.1002/ smll.202001772.
- [68] S. Tan, I. Yavuz, N. De Marco, T. Huang, S. Lee, C.S. Choi, M. Wang, S. Nuryyeva, R. Wang, Y. Zhao, H. Wang, T. Han, B. Dunn, Y. Huang, J. Lee, Y. Yang, Steric impediment of ion migration contributes to improved operational stability of perovskite solar cells, Adv. Mater. 32 (2020), 1906995, https://doi.org/10.1002/ adma.201906995.
- [69] B. Rivkin, P. Fassl, Q. Sun, A.D. Taylor, Z. Chen, Y. Vaynzof, Effect of ion migration-induced electrode degradation on the operational stability of perovskite solar cells, ACS Omega 3 (2018) 10042–10047, https://doi.org/10.1021/ acsomega.8b01626.